International Symposium
On Turbulence and Shear Flow
Phenomena (TSFP-9)
June 30 - July 3, 2015 *Melbourne, Australia*

LARGE-SCALE, COHERENT STRUCTURES IN WIDE-ASPECT-RATIO, TURBULENT, RAYLEIGH-BÉNARD CONVECTION

P. J. Sakievich, Y. T. Peet, R. J. Adrian
School for Engineering of Matter, Transport and Energy
Arizona State University
Tempe, Arizona 85287-6106, USA
psakievi@asu.edu

ABSTRACT

Investigation of the spatial organization of large-scale, coherent structures in turbulent, Rayleigh-Bénard convection is performed through direct numerical simulation. The simulation is performed in a 6.3 aspect ratio cell with a Rayleigh number of 9.6×10^7 and Prandtl number equal to 6.7. Single and double point statistics are compared against experimental results and are found to be in excellent agreement. Large-scale mean thermals with coherence times exceeding 10 eddy-turnovers are discovered and these mean thermals are found to be a reliable tool for identifying and interpreting the large, velocity roll-cells. Our simulations show an existence of a large-scale coherent pattern that consists of three major velocity roll-cells, two of which are semi-toroidal, or horse-shoe shaped, that are connected to the side-walls, and the third roll-cell lies across the center of the cell between the semi-toroidal cells. We present the possible formation mechanism of this nearly-periodic structure, observed at intermediate scales of averaging, as a perturbation from a perfectly periodic, crystal-like, pattern. The dynamics of these structures are evaluated using short-time averages.

INTRODUCTION

Rayleigh-Bénard convection (RBC) occurs when a fluid is heated from below and cooled from above in a uniform manner. It is considered to be one of the canonical turbulent flows, and it has been a subject of interest in the thermal turbulence community for decades. A large portion of recent research has focused on how the global statistics and mean profiles of RBC scale throughout the turbulent regime. Noticeably less work has been published on the characterization and life cycle of the coherent structures, despite the fact that production of turbulence by buoyancy in RBC is one of the more easily conceptualized mechanisms among all of the canonical flows. The coherent structures that occur on various scales of the flow encapsulate the principle mechanisms of turbulence in an idealized model that is physical, visual and intuitive. This fundamental level of understanding and observation provides an important foundation for data analysis, as well as advancing theories and models.

One of the most detailed descriptions of turbulent RBC structures is provided by Zocchi *et al.* (1990). They describe five characteristic structures: plumes, thermals, waves, swirls and a large-scale circulation (LSC). The plumes are either thermal columns that rise out of the thermal boundary layers or sheets near the boundary layer. The sheet-like plumes have a tendency to merge when they are in close proximity to one another (Puthenveettil & Arakeri, 2005). Shishkina & Wagner (2007) performed an extensive computational study of the sheet-like plumes to provide detailed descriptions of their geometric and physical characteristics.

Thermals are detached packets of fluid, or blobs that ascend or descend depending upon their temperature. These structures generally form when the stem of a thermal mushroom becomes too thin, and the head of the plume breaks off. Zocchi also identified another structure known as swirls where the thermal emission would curl back on itself. Models suggest that swirls arise from the same instability as plumes, but that the swirl has more shear acting in the upwind direction (Shelly & Vinson, 1992). When plumes and thermals impact the opposing boundary layer a wave is generated that propagates out from the point of impact. Zocchi shows that these waves tend to propagate toward areas where the horizontal velocities decrease and vertical velocities dominate. The regions of large vertical motion generate LSC (Qui & Tong, 2001) which are sometimes described as "roll-cells."

These structures can be classified by their spatial size and coherence times. Thermal plumes, mushroom thermals and swirls can be considered small scale structures with relatively short coherence times. The roll-cells or large-scale-circulations are aptly named since they are a much larger structures with coherence times that significantly exceed those of thermal plumes. The thermal sheets can be considered an intermediate structure since they form as a result of the interaction between roll-cells and the small-scale thermals. This range of fine, intermediate and large-scale structures provides an interesting analogy to the range of coherent structures found in shear-flows (Adrian *et al.*, 2000).

When the aspect-ratio (AR) of a convection cell is small ($AR \leq 2$), a single LSC is the largest observable structure in the flow. However, when the AR exceeds roughly 4 the LSC becomes a three-dimensional, multi-roll structure (du Puits *et al.*, 2007; Xia *et al.*, 2008). This is an important observation, since the smaller scale structures are believed to be intricately tied to the roll-cells. However, little is known about the properties of the multi-roll cell because

most analyses of coherent structures in RBC have been performed in small AR domains ($AR \leq 2$).

In this work we evaluate how multiple roll-cells interact with one another in a three-dimensional domain by focusing on the large scale velocity and thermal structures. We also evaluate the dynamics of these scales over small averaging times to determine the level of spatial coherence as a function of time.

NUMERICAL METHODOLOGY

Direct numerical simulation (DNS) of a cylindrical, turbulent, RBC cell with an AR of 6.3 was performed using the spectral element code Nek5000. Nek5000 is a highly parallelizable and well-vetted code for solving the incompressible, Navier-Stokes equations, and it currently has over 225 world-wide users (Fischer *et al.*, 2015). In this work we used the non-dimensional form of the Boussinesq equations:

$$\nabla \cdot \mathbf{u} = 0, \tag{1}$$

$$\mathbf{u}_t + (\mathbf{u} \cdot \nabla)\mathbf{u} = -\nabla p + \sqrt{\frac{Pr}{Ra}}\nabla^2 \mathbf{u} + \theta \hat{z}, \tag{2}$$

$$\theta_t + (\mathbf{u} \cdot \nabla)\theta = \frac{1}{\sqrt{RaPr}}\nabla^2 \theta, \tag{3}$$

where $\mathbf{u}$, p and θ are velocity, pressure and temperature. Equations 1-3 were scaled spatially by the height of the cell (z^*), thermally by the temperature difference between the top and bottom plates (ΔT), and the velocity was scaled by the "free-fall velocity,"

$$w_f = \sqrt{z^* g \beta \Delta T}. \tag{4}$$

The Rayleigh (Ra) and Prandtl (Pr) numbers in equation 2 are defined as:

$$Ra = \frac{\beta g \Delta T {z^*}^3}{\alpha \nu}, \tag{5}$$

$$Pr = \frac{\nu}{\alpha}, \tag{6}$$

where β, g, α and ν are the coefficients of thermal expansion, gravitational constant, thermal diffusivity and kinematic viscosity respectively. The parameters of this simulation were selected to allow direct comparison to the experiments conducted by Fernandes (2001). Fernandes conducted a series of experiments in a 6.3 AR test cell with cylindrical side-walls. These experiments were conducted with water as the working fluid and Rayleigh numbers ranging from $5.8 \times 10^7 - 1.1 \times 10^9$. Our simulation was conducted with Prandtl and Rayleigh numbers of 6.7 and 9.6×10^7 respectively. The simulation's boundary conditions were no-slip at all walls, constant temperature at the top and bottom plates and zero heat-flux along the side walls.

The simulation was gradually ramped up to the target Rayleigh number, and was allowed to reach a stable, fully-developed state before data was collected. The simulation was judged to be fully developed when the volume-averaged, kinetic energy in the cell reached a steady value. The eddy-turnover time for the roll-cells (ε_t) was estimated as the time it takes for a particle to cross the layer-depth twice:

$$\varepsilon_t = \frac{2z^*}{< w_{rms} >_v}, \tag{7}$$

where $< w_{rms} >_v$ is the volume-averaged, vertical, r.m.s. velocity. The DNS data used for analysis in this paper spanned approximately 11 of these eddy-turnover's and accounts for approximately 23 minutes in dimensional time. Brown *et al.* (2005) identified a random reorientation of the LSC in a unit AR cell that occurred on a time scale of approximately once per 10 eddy-turnovers. Fernandes (2001) also identified coherence in the large-scale structures that met or exceeded 10 eddy-turnovers. Based off these observations 10 ε_t was determined to be a scale of interest, and in the context of this paper it is treated as a medium, or intermediate temporal scale.

The spatial domain was discretized with hexahedral elements and a marginal amount of biasing toward the upper and lower plates was applied to the element distribution. The spectral element method (SEM) used in this simulation also applies a Gauss-Lobatto-Legendre (GLL) quadrature which clusters points inside each element toward the boundaries. Ninth order polynomials were used for the quadrature and the total number of grid points in the simulation accounted to roughly 44 million. Fernandes calculated the Kolmogorov length for this scenario to be approximately $1.2 \times 10^{-2} z*$ and simulation's grid had 5 points within this range at the wall. The temporal resolution for each time step was approximately $\varepsilon_t/10000$ with a corresponding CFL range of $\sim 0.6 - 0.7$.

VALIDATION

Validation of the simulation was performed by comparing single and double point statistics with the experimental results of Fernandes (2001). Fernandes obtained velocity statistics through the use of two-dimensional, particle image velocimetry (PIV). The PIV measurements were taken at a vertical plane in the center of the cell with a field of view of 1.85 z^* in length and 1 z^* in height. It should be noted that Fernandes performed dimensionless analysis using the Deardorf scales, and his selected length scale was half the layer depth (0.5 z^*). The Deardorf scales were selected due to their excellent scaling properties as outlined by Adrian *et al.* (1986). The Deardorf velocity and temperature scales are listed below where Q_o is the kinematic heat flux,

$$w^* = (\beta g Q_o z^*)^{1/3}, \tag{8}$$

$$\theta^* = \frac{Q_o}{w^*}. \tag{9}$$

This simulation used the "free-fall" scales during the calculations because they provide better accommodation for the constant temperature boundary conditions. However, all velocity data presented in this paper was rescaled to the Deardorf scales to provide a one-to-one comparison of velocity statistics with Fernandes. This was accomplished by multiplying the field by w_f and then dividing by w*. The value used for w* (2.5 mm/s) was obtained from data published by Fernandes at the Rayleigh number 9.6×10^7.

Fernandes' statistics were generated from a set of 300 statistically independent snapshots which were obtained over very long averaging times. These snapshots were collected in groups of 15 with $4z^*/w^*$ (~30-40 seconds) between each snapshot. The heat source was periodically turned off for 30 minutes to an hour between sets of snapshots, then turned back on and allowed to settle for 4-12 hours. This perturbing of the flow was done to keep the large-scale-motions from developing any preferential direction so the horizontal planes could be considered statistically homogeneous in the cell's core.

Recreating a DNS data set that spans a similar amount of time with similar perturbations would be prohibitively expensive. However, DNS results can expand the usable data when the assumption of horizontal homogeneity is applied. This is because of the additional spatial dimension that is present in the three-dimensional data set. Fernandes applied ensemble and horizontal-line averages to 2D PIV data sets to examine velocity statistics across horizontal planes. The same averaging procedures were applied to the DNS data over the same viewing window as Fernandes. The only modification that was made for the DNS results was to convert the spatial line-average into a plane-average to reproduce the same statistics over a shorter run time.

SINGLE-POINT STATISITICS

Single-point, velocity statistics for the r.m.s. velocity components along the z-direction are used to compare the simulation results with the experiments of Fernandes. The w-velocity statistics in figure 1 show excellent agreement with Fernandes' data. The horizontal components of the

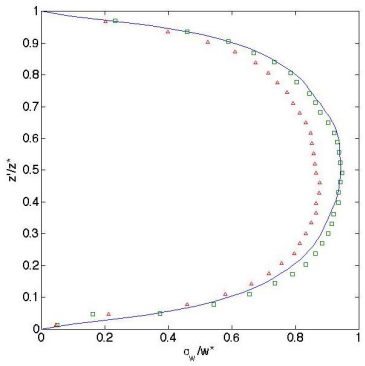

Figure 1: Ensemble and horizontally averaged r.m.s. vertical velocity profile normalized by w*: DNS: Ra=$1x10^8$ (–); Experiment: Ra=$6x10^7$ (△), Ra=$2x10^8$ (□)

velocity field also show good agreement with experimental data. The discrepancy between the u and v r.m.s components within the simulation results is believed to be because of the total averaging time. 11 eddy-turnovers is an intermediate span of time to perform averages and these profiles should become increasingly similar as the averaging time is increased.

TWO-POINT STATISITICS

Two-point, correlation functions of the velocity field for vertical separation are compared against the published results of Fernandes. This statistic is a useful mechanism

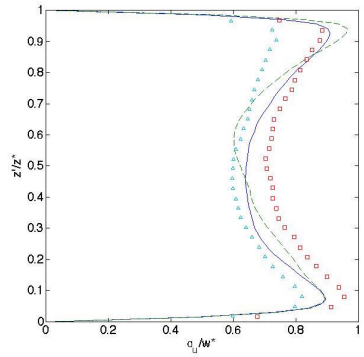

Figure 2: Ensemble and horizontally averaged r.m.s. horizontal velocity profiles normalized by w*: DNS: Ra=1×10^8 $\sigma_u/w*$ (–), $\sigma_v/w*$ (- -); Experiment: Ra=6×10^7 (△), Ra=2×10^8 (□)

for analyzing similarity in the spatial structure of the velocity field and is a good metric to judge how the organization of our DNS velocity field compares with the experiments'.

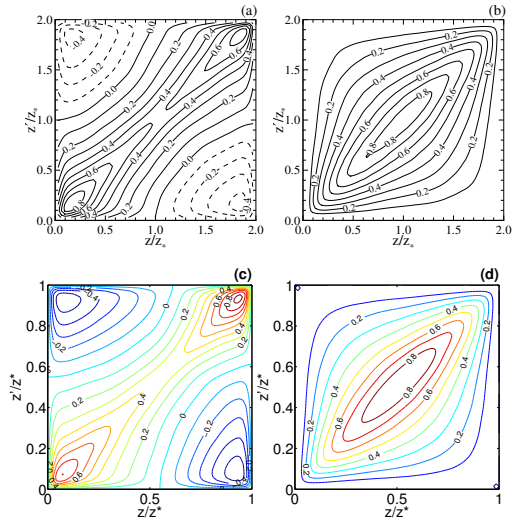

Figure 3: Contour plot of the vertical, two-point correlation of the u-velocity component (left) $< u(z)u(z') >$ and w-velocity component $< w(z)w(z') > (right)$: (a) and (b) experimental results at Ra=2×10^8, (c) and (d) DNS at Ra=1×10^8

Figure 3 shows excellent agreement between the experimental and DNS spatial correlations for the w and u velocity components. The DNS v-velocity correlation is omitted from this section because it is virtually the same as the u-correlation displayed in figure 3. Excellent agreement between the DNS and experimental results shows that increased spatial data can indeed be used to reconstruct long-time average statistics in the center of the RBC cell. This also supports Fernandes' conclusion that over long averaging times these statistics are homogeneous, or at the very least axisymmetric along horizontal planes.

LARGE-SCALE STRUCTURES

Large-scale structures can be clearly seen through time-averaged data if the averaging time is of the order of

their coherence times. Typically large-scale structures in RBC, such as the LSC's, are analyzed through the velocity field. However, this investigation will begin with the temporally averaged temperature field. The figures in this section present data that has been averaged over the full time span of the DNS simulation ($\sim 11\varepsilon_t$). We shall refer to these as 'mean' fields, bearing in mind that they are different from the classical mean fields that would be obtained by averaging over infinite time.

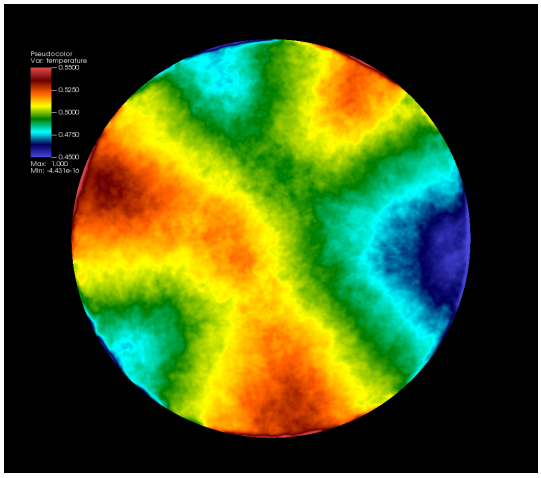

Figure 4: Average temperature field at $z* = 0.5$ scaled between 0.45-0.55ΔT

The results in figure 4 show a striking set of triangular patterns for the mean thermals that are manifest at the mid-plane. These large-scale structures can be interpreted as the areas where high concentrations of thermal plumes rise and fall over time. The mid-plane is an ideal location to investigate the mean-thermal structures because the mean horizontal velocity components are minimal, and the up (warm) and down (cool) motions are comparable due to symmetry about the mid-plane. Connecting the warm and cool thermals creates a complete roll-cell. This basic method can be used to conceptualize the 3D multi-roll-cell pattern in a simple and intuitive manner.

Coupling between the mean thermal field and the velocity roll-cells is further illustrated by comparing the spatial locations of the mean velocity up/down drafts and the vector field connecting these drafts. Figure 5 uses iso-surfaces to illustrate the location of the mean vertical-drafts, and a vector field at the plane $z* = 0.85$ to show how the drafts are connected to one another. A comparison of figures 4 and 5 clearly shows that from this perspective the warm thermals represent velocity sources and the cool thermals represent velocity sinks.

SPATIAL ORGANIZATION OF THE LARGE-SCALE STRUCTURES

Understanding the relationship between mean-thermals and roll-cells lays the foundation for analysis of the spatial organization of the multiple roll-cell pattern. Seven discrete, mean-thermals can be identified in figure 4. Six of the seven thermals are connected to the cell's side walls, and are alternately arranged by temperature. The

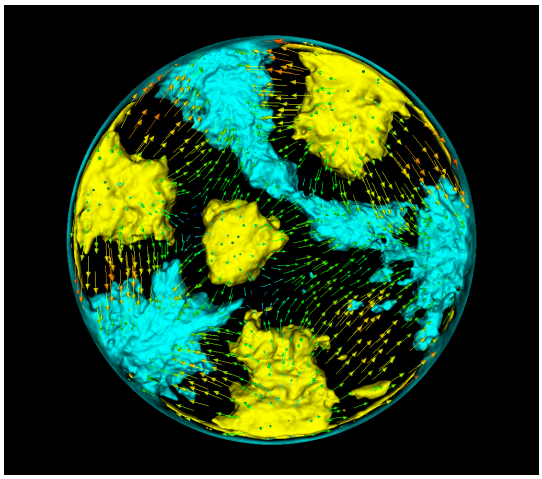

Figure 5: Iso-surface of the vertical velocity component (yellow=0.3 w*; blue =-0.3 w*) with velocity vectors at z*=0.85 colored by velocity magnitude

seventh thermal is warm updraft located in the central region of the cell, centered about the x-y point (-0.5,0.0). The roll-cell organization in this case can be described by three major circulations: two partial toroids that are centered around up and down drafts on the walls and a third roll-cell between them. The central roll-cell is compressed in the center of the convection cell where the peak of the toroids meet and it expands near the walls. Figure 6 provides a conceptual illustration of this net effect.

It should be noted that no preferential alignment is indicated by the governing equations, circular geometry, or boundary conditions and so an ensemble average over sufficiently many instances of the flow should generate axisymmetric statistics, that is it should be statistically homogeneous with respect to shifts in the azimuthal direction. If one were to ensemble average fields like those in figures 4 and 5 from many separate instances of the flow the recovered results would approach axisymmetry because there is nothing to constrain the orientation between instances. If the flow is truly statistically stationary then the time average has to reach the same result as the ensemble average over a sufficiently long averaging time.

The medium-time averaged data shown in figures 4 and 5 is clearly not axisymmetric. The pattern seen in these figures is much closer to 120° azimuthal periodicity than axisymmetry. There are several interesting departures from pure periodicity that can be observed in medium-time average data such as the central thermal residing off the central axis and the size variation amongst the thermals along the outer wall. Figures 4 and 5 obviously contains noise due to averaging over a finite time. If one were to ensemble average many patterns like those in figures 4 and 5 keeping them aligned in the azimuthal direction, a periodic pattern would arise that is consistent with the period three behavior of the up-flows, down-flows and central column of rising fluid.

Figure 7 conceptually illustrates this periodic pattern. It shows a hub and spoke pattern with roll-cells forming between alternating thermals around the outer wall and vortex lines located between the thermals. The central uprising thermal creates in-plane, azimuthal vorticity due to the shearing effects, manifested as a circular vortex ring around it. This vorticity acts to reinforce the interaction of the mean thermal with the side thermals of opposing temperature and

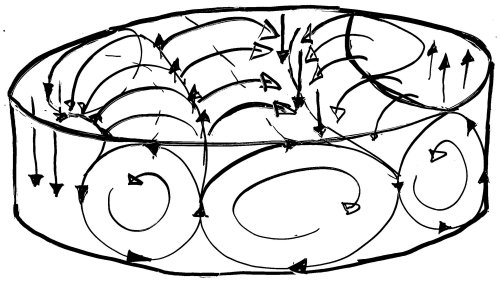

Figure 6: Conceptual sketch of the three dimensional, multi-roll cell organization seen in the DNS results.

to strengthen the global large scale motions observed in the simulations.

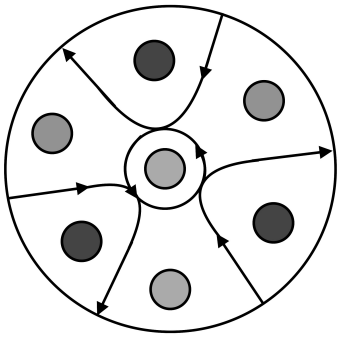

Figure 7: Conceptual diagram of the possible periodic multi-roll cell organization. The light circles represent updrafts, the dark circles represent downdrafts and the vectors represent vortex lines.

The differences between the roughly periodic visualizations and the perfectly periodic conceptualization of figure 7 can be explained as a perturbation from an ideal state. When the location of the central thermal moves off the center axis it automatically comes closer to two other thermals with similar temperatures. This shift breaks the symmetry, enhances the interaction between the central thermal and the nearest thermal of opposing temperature, and could cause the other two vortex lines to break and reform as sketched in figure 8.

Comparison of figures 4-8 shows excellent continuity between the conceptual descriptions and the numerical results. It is recognized that this pattern is most likely a function of AR and that additional patterns may exist at other AR's and in other domains.

DYNAMICS OF THE LARGE SCALE STRUCTURES

One drawback of examining a time averaged field is that the averaging operator filters out the details of structures that are not supported over long coherence times. This filtering makes it difficult to determine if a structure is simply an artifact of multiple structures that are smeared together, or if it is truly coherent across the entire time scale. For example, if the thermal pattern seen in figure 4 were to arbitrarily rotate around the central axis, then a very, long-time average at the mid plane would yield a constant thermal field of $0.5\,\Delta T$ along the outer edges and a central warm spot in the middle. A very long-time average pattern like this could be associated with a single toroid. However, this would not mean that the thermal pattern described in previous sections ceased to exist; it would just mean there was an inherent dynamic that makes the multi-roll cell pattern indiscernible in a very long-time average. Nothing in the geometry or governing equations constrains the flow, and so the mean-thermals and roll-cells should be evaluated at relatively small time-scales to determine their dynamics.

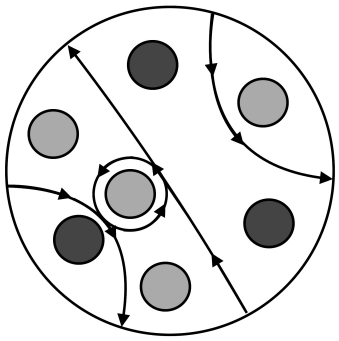

Figure 8: Conceptual diagram of the multi-roll cell organization seen in the DNS results as a perturbation of the possible periodic pattern. The light circles represent updrafts, the dark circles represent downdrafts and the vectors represent vortex lines.

Averages once every ε_t were performed to evaluate the short-time dynamics of these structures since this is, roughly, the minimum coherence time for a roll-cell. The short-time-averaged temperature field and vertical-velocity iso-surfaces are presented in figure 9. These instances were taken 3 ε_t apart to increase the dynamic effect through static visualizations. Very little change is observed in the thermal field which shows that the mean thermals are relatively stationary over the averaging time of this data set. Slightly more variance is observed in the vertical-velocity iso-surfaces, but most of the changes are observed in the central region of the cell. The up and down drafts near the walls show little change in spatial location. This indicates that the 3 roll-cell pattern depicted in figures 6 and 8 is remarkably stable across this time scale.

CONCLUSIONS AND FUTURE WORK

It has been shown that large-scale mean thermals exist in turbulent RBC on a time scale of 11 eddy turn-over times, and that these mean thermals are closely connected to the mean vertical velocity drafts in the convection cell. Connecting opposing mean thermals has been identified as a novel and conceptually simple way to visualize the mean roll-cells. It has also been shown that these mean thermals can be dynamically stable within the time scale of $11\varepsilon_t$ for a 6.3 AR cell at the given Rayleigh and Prandtl numbers. The roll-cell organization for this case is believed to consist of three roll-cells that are aligned by the mean thermals. Future works for this investigation include collecting and evaluating data over longer run times to explore additional large-scale dynamics, and proper orthogonal decomposition of the flow field to validate the characteristic patterns.

We would like to acknowledge U. S. National Science Foundation Grants CBET-1335731 and CMMI-1250124 as well as the Arizona State University Dean's Fellowship for supporting this work.

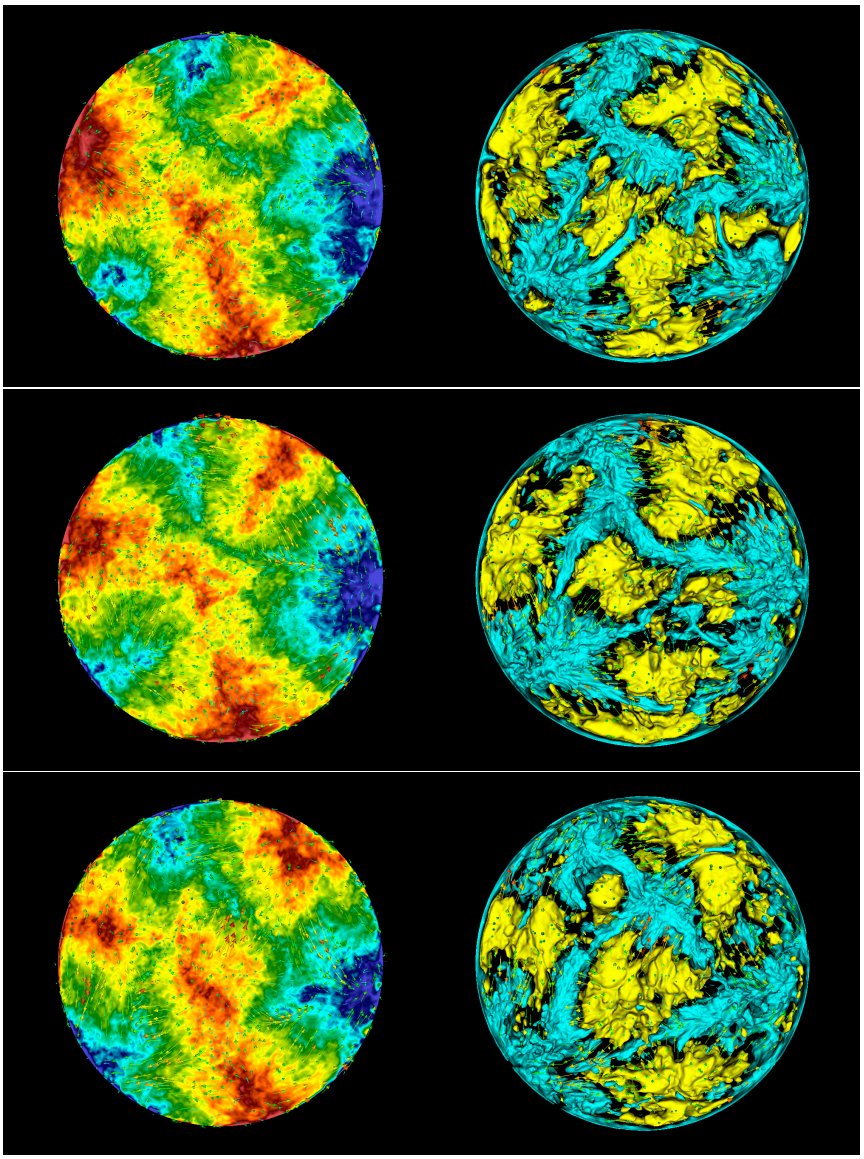

Figure 9: Thermal field at the mid-plane scaled from $0.45 - 0.55\Delta T$ (left); velocity iso-surfaces where yellow is 0.3 w* and blue is -0.3 w* (right); averaged once per ε_t and ordered in time from top to bottom

REFERENCES

Adrian, R. J., Christensen, K.T. & Liu, Z.C. 2000 Analysis and interpretation of instantaneous turbulent velocity fields. *Experiments in Fluids* **29** (3), 275–290.

Adrian, R. J., Ferreira, R. T. D. S. & Boberg, T. 1986 Turbulent thermal convection in wide horizontal fluid layers. *Experiments in Fluids* **4**, 121–141.

Brown, E., Nikolaenko, A. & Ahlers, G. 2005 Reorientation of the large-scale circulations in turbulent rayleigh-benard convection. *Physical Review Letters* **95** (084503).

Fernandes, R. L. 2001 The spatial structure of turbulent rayleigh-benard convection. PhD thesis, University of Illinois at Urbana-Champaign, Urbana, IL.

Fischer, P. F., Lottes, J. W. & Kherkemeir, S. G. 2015 nek5000 web page, https://nek5000.mcs.anl.gov/.

du Puits, R., Resagk, C. & Thess, A. 2007 Breakdown of wind in turbulent thermal convection. *Physical Review E* **75** (016302).

Puthenveettil, B. A. & Arakeri, J. 2005 Plume strucutre in high rayleigh-number convection. *Journal of Fluid Mechanics* **542**, 217–249.

Qui, X. L. & Tong, P. 2001 Large-scale structures in turbulent thermal convection. *Physical Review E* **64** (036304).

Shelly, M. J. & Vinson, M. 1992 Coherent structures on a boundary layer in rayleigh-benard turbulence. *Nonlinearity* **5**, 323–351.

Shishkina, O. & Wagner, C. 2007 Analysis of sheet-like thermal plumes in turbulent rayleigh-benard convection. *Journal of Fluid Mechanics* **599**, 383–404.

Xia, K. Q., Sun, C. & Cheung, Y. H. 2008 Large scale velocity structures in turbulent thermal convection with widely varying aspect ratio. *Proc. 14th Int. Symp. On Applications of Laser Techniques to Fluid Mechanics* .

Zocchi, G., Moses, E. & Libchaber, A. 1990 Coherent structures in turbulent convection, an experimental study. *Physica A* **166**, 387–407.